Self-organization of shear bands in titanium and Ti–6Al–4V alloy

Q. Xue, M.A. Meyers [*], V.F. Nesterenko

Department of Mechanical and Aerospace Engineering, University of California, San Diego, 9500 Gilman Drive, La Jolla, CA 92093-0411, USA

Abstract

The evolution of multiple adiabatic shear bands was investigated in commercially pure titanium and Ti–6Al–4V alloy through the radial collapse of a thick-walled cylinder under high-strain-rate deformation ($\sim10^4$ s^{-1}). The shear-band initiation, propagation, as well as spatial distribution were examined under different global strains. The shear bands nucleate at the internal boundary of the specimens and construct a periodical distribution at an early stage. The shear bands are the preferred sites for nucleation, growth, and coalescence of voids and are, as such, precursors to failure. The evolution of shear-band pattern during the deformation process reveals a self-organization character. The differences of mechanical response between the two alloys are responsible for significant differences in the evolution of the shear band patterns. The number of shear bands initiated in Ti (spacing of 0.18 mm) is considerably larger than in Ti–6Al–4V (spacing of 0.53 mm); on the other hand, the propagation velocity of the bands in Ti–6Al–4V (~556 m/s) is approximately three times higher than in Ti (~153 m/s). The experimental shear-band spacings are compared with theoretical predictions that use the perturbation analysis and momentum diffusion; the shortcomings of the latter are discussed. A new model is proposed for the initiation and propagation that incorporates some of the earlier ideas and expands them to a two-dimensional configuration. The initiation is treated as a probabilistic process with a Weibull dependence on strain; superimposed on this, a shielding factor is introduced to deal with the deactivation of embryos. A discontinuous growth mode for shear localization under periodic perturbation is proposed. The propagating shear bands compete and periodically create a new spatial distribution. © 2002 Published by Elsevier Science Ltd on behalf of Acta Materialia Inc.

Keywords: Shear bands; Self-organization; Titanium; Ti-6Al-4V alloy

1. Introduction

Shear localization is an important and often dominating deformation and failure mechanism at high strain rates e.g. [1] and [2]. It has been the object of numerous studies, focused both on the mechanics and microstructural aspects of the process. The constitutive equations governing adiabatic shear localization are well known, and the approaches developed by Clifton [3], Bai [4], Molinari and Clifton [5], Wright [6], and Wright and Walter [7] successfully predict the strains for the

* Corresponding author. Tel.: +1-858-534-4719; fax: +1-858-534-5698.

E-mail address: mameyers@mae.ucsd.edu (M. Meyers).

initiation as well as other parameters, such as band thickness. These analyses have been corroborated by controlled, instrumented experiments; prominent among those are the pioneering results by Marchand and Duffy [8]. From a microstructural evolution viewpoint, a number of structural alterations, including dynamic recovery, dynamic recrystallization, phase transformations, and melting/resolidification have been observed. For titanium and titanium alloys, Schechtman et al. [9], Grebe et al. [10], Meyers and Pak [11], Meyers et al. [12], and Timothy and Hutchins [13,14], have identified important microstructural alterations. Ramesh and coworkers [15–17] have recently investigated Ti and Ti alloys.

However, the great majority of studies addressed an individual shear band. Exceptions are the studies by Bowden [18] and Shockey [19] showing multiple shear bands and emphasizing their spacing. It was shown by Nesterenko et al. [20] that shear bands in titanium exhibit a self-organization behavior with a characteristic spacing. These observed spacings were compared with the three existing Grady–Kipp [21] and Wright–Ockendon [22] and Molinari [23] theories. One of the objectives of this report is to expand on the initial findings [20] and to propose a new, two-dimensional treatment for the self-organization of shear bands. The role played by shear bands in the initiation and evolution of damage is also characterized. Titanium and Ti–6Al–4V alloy were chosen because they both have close compositions, density, and a demonstrated propensity for shear localization but have rather different mechanical properties; the yield strength of Ti–6Al–4V is approximately twice that of Ti.

2. Theoretical predictions

A few theoretical predictions for spacing of shear bands have been proposed to characterize the spatial distribution of shear bands. Since the evolution of multiple shear bands is very complex due to the interactions among them, most analyses are still simplified under one-dimensional simple shear condition.

Grady [24] was the first to propose a pertur-

bation solution to shear instability of brittle materials. The governing equations were simplified as a dimensionless system. The principle of perturbation analysis is shown in Fig. 1. The schematic process reveals the development of perturbations in an initially homogeneous deformation. The competition among small perturbations produces a new distribution of perturbations with larger amplitudes. In Fig. 1, two wavelengths (L_1 and L_3) are shown. The amplitude of the perturbation with larger wavelength (L_3) grows faster and dominates the process at t_3. Shear bands evolve from the growth of perturbations. A Newtonian viscous constitutive equation was used to describe the shear deformation of the solid medium:

$$\tau = \eta(T)\frac{\partial v}{\partial y}, \tag{1}$$

where τ is the shear stress, v is the velocity, and the viscous coefficient $\eta(T)$ is temperature dependent:

$$\eta(T) = \eta_0 \exp[-a(T-T_0)], \tag{2}$$

η_0 and T_0 are a material constant and the reference temperature, respectively. The perturbation wavelength associated with the instability corresponds to the minimum spacing. The following characteristic wavelength was obtained from the perturbation analysis:

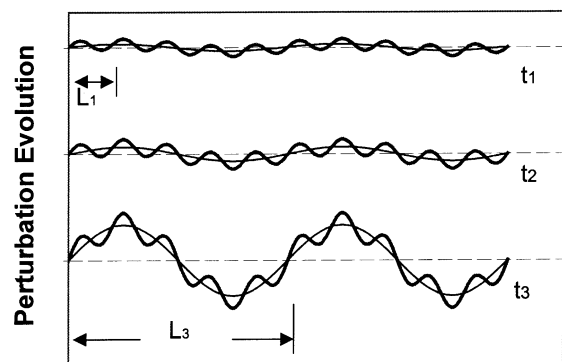$$L_G = \frac{2\pi}{\dot{\gamma}_0}\left[\frac{kC}{a^2\eta_0}\right]^{1/4}. \tag{3}$$

Fig. 1. Schematic of evolution perturbations with development of characteristic spacing for subsequent shearband nucleation.

Grady and Kipp [21] later proposed another approach (called here the GK model) to determine spatial distribution of shear bands. They extended Mott's [25] early analysis for dynamic fracture. Mott [25] pointed out that the velocity of stress release away from the point of fracture was controlled by momentum diffusion and was much lower than elastic wave velocity. Fig. 2 gives the deformation distribution under one-dimensional simple shear and shows in a schematic manner the principle of momentum diffusion. The momentum diffusion due to the unloading creates a rigid region between the shear band and the plastic deformation region. The rigid–plastic interface propagates at a speed lower than the elastic wave velocity. A linear relaxation of stress was used to describe approximately the relation of unloading stress. A simple constitutive equation, $\tau = \tau_0[1 - a(T - T_0)]$, was applied; a is a softening parameter. Work hardening and strain rate sensitivity are neglected. Grady and Kipp [21] indicated that the shear band spacing should correspond to the minimum localization time during which the shear band

reached its critical width. The predicted spacing, L_{GK}, is:

$$L_{GK} = 2\left[\frac{9kC}{\dot{\gamma}_0^2 a^2 \tau_0}\right]^{1/4}. \qquad (4)$$

Wright and Ockendon [22] developed their theoretical model (WO model), based on the analysis of small perturbations. The basic concept is similar to Grady's earlier work [24]. The following constitutive equation for a rate dependent material was used:

$$\tau = \tau_0[1 - a(T - T_0)]\left(\frac{\dot{\gamma}}{\dot{\gamma}_0}\right)^m, \qquad (5)$$

where m is the strain rate sensitivity. The spacing of shear bands, L_{WO}, is:

$$L_{WO} = 2\pi\left(\frac{m^3 kC}{\dot{\gamma}_0^2 a^2 \tau_0}\right)^{1/4}. \qquad (6)$$

More recently, Molinari [23] modified the WO model by adding strain hardening:

$$\tau = \mu_0(\gamma + \gamma_i)^n \dot{\gamma}^m T^\nu. \qquad (7)$$

μ_0 and ν are constants and γ_i is a pre-strain, and m is the strain-rate sensitivity and n is the strain hardening exponent. The predicted spacing of shear bands is:

$$L_M = \frac{2\pi}{\xi_0}\left[1 + \frac{3}{4}\frac{\rho c \frac{\partial \dot{\gamma}}{\partial \gamma}}{\beta \tau_0 \frac{\partial \dot{\gamma}}{\partial T}}\right]^{-1}, \qquad (8)$$

where ξ_0 is the wave number. For a non-hardening material, the Molinari model takes the simple form:

$$L_M' = 2\pi\left[\frac{kCm^3(1 - aT_0)^2}{(1 + m)\dot{\gamma}_0^2 a^2 \tau_0}\right]^{1/4}. \qquad (9)$$

Eq. (7) for linear thermal softening can be rewritten as:

$$\dot{\gamma} = \tau^{1/m}[\mu_0(1 - aT)]^{-1/m}(\gamma + \gamma_i)^{-n/m}. \qquad (10)$$

The initial wave number ξ_0 is obtained directly from the non-hardening solution of shear band spacing:
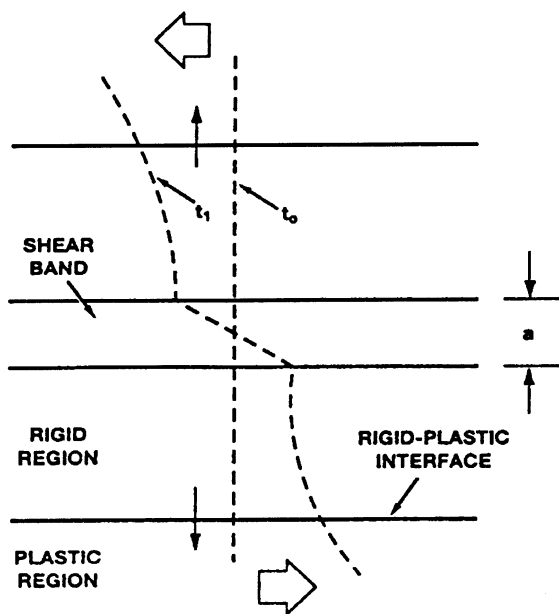

Fig. 2. Structure of one-dimensional shear band and stress release behavior in the vicinity of the shear band. Note that rigid regions and plastic flow regions are separated by a propagating interface (adapted from Grady and Kipp [21]).

$$\xi_0 = \frac{2\pi}{L_M{}'}. \tag{11}$$

The spacing of shear band with work hardening effect is obtained by substituting Eqs. (8) and (10) into Eq. (11):

$$L_M = \left[1 - \frac{3}{4}\frac{\rho c}{\beta \tau_0^2}\frac{n(1-aT)}{\beta a \gamma}\right]^{-1} \cdot \left[\frac{kCm^3(1-aT_0)^2}{(1+m)\dot{\gamma}_0^2 a^2 \tau_0}\right]^{1/4}, \tag{12}$$

where the pre-strain is assumed to be zero, $\gamma_i=0$.

The above predictions are classified into two types: momentum diffusion to describe the later stage of the shear localization [21], and the perturbation analysis to explain the initial growth of shear bands at an early stage [22–24]. They can also be expressed as:

Grady − Kipp

$$L = 2\pi \left[\frac{kC}{\dot{\gamma}^3 a^2 \tau_0}\right]^{1/4} \cdot \frac{9^{1/4}}{\pi} \tag{13}$$

Wright − Ockendon

$$L = 2\pi \left[\frac{kC}{\dot{\gamma}^3 a^2 \tau_0}\right]^{1/4} \cdot m^{3/4} \tag{14}$$

Molinari

$$L = 2\pi \left[\frac{kC}{\dot{\gamma}^3 \tau_0 a^2}\right]^{1/4} \cdot \left[\frac{m^3(1-aT_0)^2}{(1+m)}\right]^{1/4}$$
for $n = 0$. $\tag{15}$

The WO and Molinari models are the same except for a factor $[(1-aT_0)^2/(1+m)]^{1/4}$. Since m is much less than 1 and T_0 is the reference temperature, this factor is approximated as $(1-aT_0)^{1/2}$. The form of the equations enables direct comparison between the three predictive models. Generally speaking, if the strain hardening effect is ignored, the Molinari prediction is of the same order as the WO model, except for the coefficient. The coefficient in the GK model is independent of work hardening. Under such an extreme condition, the absence of strain-rate sensitivity in the GK model does not affect the distribution of shear bands, although we can incorporate the strain rate term into the constitutive equation by obtaining τ_0 from Eq. (7). The coefficient of GK model is 0.55, which is at least 5 to 10 times larger than $m^{3/4}$ since m is about 10^{-2} for most metals.

3. Materials and experimental procedure

3.1. Materials and constitutive behavior

Commercially pure titanium is a typical high purity α titanium with HCP structure. Titanium undergoes an allotropic transformation from HCP (α-Ti) to BCC (β-Ti) at about 882°C. Nesterenko et al. [20] used this material to examine the spatial distribution of shear bands. In the present research, the former cylindrical specimens after collapse were re-examined for the detailed characterization of shear localization.

Ti–6Al–4V alloy, in the form of a rod 1 inch in diameter, was used (ASTM B348-95 with grade 5). It was in the annealed condition (705°C for two hours and air cooling), providing a two-phase structure with elongated grains. The grain size is about 7 μm length and 3 μm width.

The constitutive response of the materials used was described by means of Zerilli–Armstrong (Z–A) equations. Quasi-static and dynamic tests were conducted to obtain the Z-A parameters. The thermal softening parameters α_0, α_1, β_0 and β_1 were taken directly from Zerilli and Armstrong [26]. Zerilli and Armstrong extended their theoretical prediction, initially developed for BCC [27] and FCC [28] metals, to HCP [26]. They pointed out that HCP metals have a mechanical response falling somewhere between BCC and FCC metals. They used a combination of predominant interactions, the Peierls stress type (BCC) and the forest dislocations type (FCC) to describe the constitutive response of HCP metals:

$$\sigma = \sigma_a + Be^{-(\beta_0 - \beta_1 \ln \dot{\varepsilon})T} \\ + B_0 \varepsilon^{C_n} e^{-(\alpha_0 - \alpha_1 \ln \dot{\varepsilon})T}. \tag{16}$$

In Eq. (16), B, B_0, β_0, β_1, α_0, α_1 and C_n are parameters. The constant σ_a represents the athermal component of the flow stress (that includes the grain size effect). The second and the third terms describe the thermal activation from the Peierls stress interaction and the intersection of dislocations, respectively. The parameters not obtained experimentally were taken from Zerilli and Armstrong [26], Chichili et al. [16,17], and Meyers et al. [12] for Grade 2 CP titanium. The prediction equation was fitted and the parameters are listed

Table 1
Parameters of Zerilli–Armstrong prediction for Ti and Ti–6Al–4V alloy

Mixed model: $\sigma = C_0 + B_0 \varepsilon^{C_n} \exp(-\alpha_0 T + \alpha_1 T \ln \dot{\varepsilon}) + B \exp(-\beta_0 T + \beta_1 T \ln \dot{\varepsilon})$								
	C_0 (MPa)	B_0 (MPa)	α_0 (K^{-1})	α_1 (K^{-1})	C_n	B (MPa)	β_0 (K^{-1})	β_1 (K^{-1})
CP Ti	0	990	1.1×10^{-4}	7.5×10^{-5}	0.5	700	2.24×10^{-3}	9.73×10^{-5}
Ti–6Al–4V	340	1135	1.4×10^{-5}	7×10^{-5}	0.5	1485	2.75×10^{-3}	7.47×10^{-5}

in Table 1. Fig. 3(a) shows a comparison of the experimental curves by Chichili et al. [16,17] and Meyers et al. [12] with the Z-A predictions for Ti. The predicted curves are in good agreement with the experimental data.

Ti–6Al–4V alloy includes both HCP (α phase) and BCC (β phase) structure. Its constitutive response depends much more on the mechanism that dominates BCC metals than titanium. The parameters are listed in Table 1. The predicted responses are compared with experimental results in Fig. 3(b). There is a good match with experimental curves. These constitutive equations were used in the prediction of the adiabatic temperature rise (Section 5.4).

3.2. Thick-walled cylinder explosion technique

The thick-walled cylinder implosion technique was introduced by Nesterenko et al. [29,30] and represents an improvement from the contained exploding cylinder technique developed by Shockey [19]. The technique is described in detail elsewhere [31,32] and will be only briefly presented here.

The specimen is sandwiched between a copper driver tube and a copper stopper tube and is collapsed inwards during the test. OFHC copper was used to make these tubes. The internal diameters of the inner copper tube were selected to produce prescribed and controlled final strains. In some special cases a central steel rod was also used. The explosive is axi-symmetrically placed around the specimen. The detonation is initiated on the top. The expansion of the detonation products exerts a uniform pressure on the cylindrical specimen and drives the specimen to collapse inward. The detonation velocity of the selected explosive is approximately 4000 m/s and the density of the explosive is 1 g/cm^3. The velocity of the inner wall of the tube was determined by an electromagnetic gage. The initial velocity of collapse of the inner tube was found by Nesterenko et al. [33] to be approximately 200 m/s.
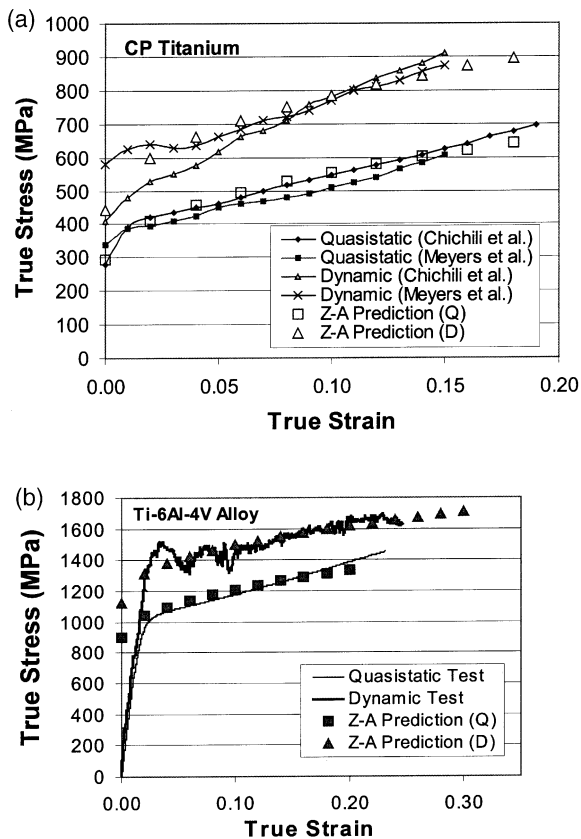
Fig. 3. Comparison between the experimental data and the Zerilli–Armstrong predictions for (a) CP titanium. Experimental data from Chichili et al. [16] (quasi-static, $\dot{\varepsilon} = 10^{-3}$ s^{-1}; dynamic, $\dot{\varepsilon} = 5\times10^3$ s^{-1}, and Meyers et al. [12] (dynamic, $\dot{\varepsilon} = 1.2\times10^3$ s^{-1}).(b) Ti–6Al–4V. Note that 'Q' and 'D' represent quasi-static and dynamic; and the corresponding strain rates are 10^{-3} s^{-1} and 3.8×10^3 s^{-1}, respectively.

It is possible to obtain an estimate of the upper bound of this velocity by a simple analytical calculation which equates the chemical energy of the explosive to the kinetic energy of the collapsing cylinder and of the detonation gases. This is the Gurney approach. An equation applicable to the geometry used here was developed by Meyers and Wang [34]. Neglecting the effect of plastic deformation work, we have:

$$V = \sqrt{2E}\left[\frac{3}{5\dfrac{M}{c} + 2\left(\dfrac{M}{c}\right)^2\dfrac{R+r}{r} + \dfrac{2r}{R+r}}\right]^{1/2}. \qquad (17)$$

V is the collapse velocity of the cylinder, E is the Gurney energy, M and c are the masses of metal and explosive charge, respectively, R is the external radius of the explosive charge (equal to 30 mm), and r is the external radius of the cylinder (equal to 15 mm). The Gurney energy was obtained through the empirical relationship by Kennedy [35]:

$$\sqrt{2E} = D/3. \qquad (18)$$

D is the detonation velocity, equal to 4000 m/s. The initial collapse velocity was equal to 366 m/s. Recent calculations using RAVEN have yielded a collapse velocity of 250 m/s. These calculations represent an upper bound and shows that the measured value of 200 m/s is reasonable. Incorporation of the plastic deformation work would reduce the calculated velocity obtained from Eq. (17).

To avoid extra wave reflection from the free interface between the stopper and the specimen, a shrink-fit technique was applied. The outer diameter of stopper was designed 0.03 mm larger than the inner diameter of the specimen. For Ti–6Al–4V alloy, special steel rods were applied to stop the radial deformation at a much earlier stage. Steel rods with diameters of 7 mm and 9 mm were used as the core at the center of cylinder specimen to stop the deformation.

The collapse of thick-walled cylinder specimen occurs in a plane strain condition. The stress state can be considered as a superposition of a hydrostatic pressure and a pure shear stress due to the axi-symmetrical geometry and loading. The maximum shear strain occurs on the internal surface of the cylindrical specimen, and thus shear bands preferentially initiate there. After each experiment, the cylinders were sectioned, ground and polished. The lengths of shear bands, l_i, the edge displacements, δ_i, the average radius of final internal boundary, R_f, and the angle between spatial position from origin, Ψ_i, were measured as shown in Fig. 4. In order to compare the deformation at the different positions on the specimen, an effective strain is used as:

$$\varepsilon_{ef} = \frac{2}{\sqrt{3}}\varepsilon_{rr} = \frac{2}{\sqrt{3}}\ln\left(\frac{r_0}{r_f}\right), \qquad (19)$$

where r_0 and r_f are the initial and final radii of a reference point. The effective global strain at the internal boundary of the specimen is considered as a characteristic value of deformation since all the specimens have the same initial dimensions. Based on the number of distinguishable shear bands, the average spacing between them is:
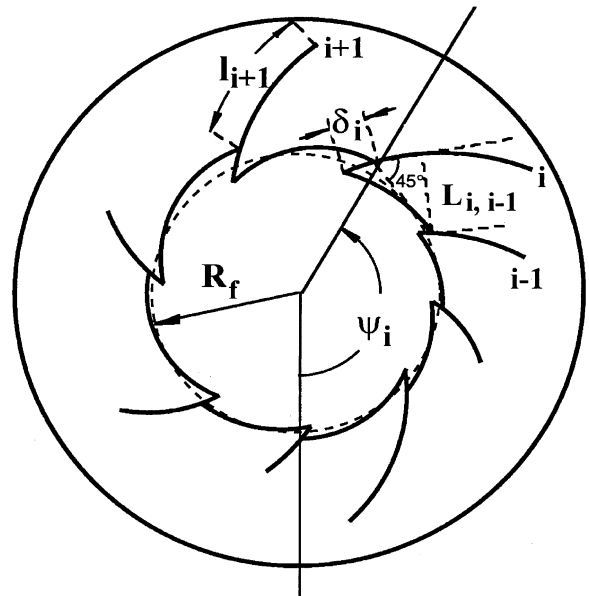
$$L = \frac{\Psi_i R_f}{n_i\sqrt{2}}, \qquad (20)$$

Fig. 4. Characteristics of shear band pattern and basic measurement; Ψ_i is the reference angle and R_f is the final radius of the collapsed cylinder; L_i is the spacing between the ith and the $i-1$ shear band, l_i is the length of the ith shear band and δ_i is its edge length.

where n_i is the number of shear bands at the particular region i and Ψ_i is the corresponding angle referring to the original angle. If $n_i = n_{total}$, $\Psi_i = 2\pi$. The spacing between shear bands decreases as plastic deformation proceeds due to the continuing deformation [36]. The measured spacings are actually the sum of the real developing part and the geometrical part due to the change of the cylinder configuration. This geometrical effect needs to be subtracted from the results by an appropriate correction. The values of spacings at the initiation of the bands was taken as a reference. The spacing of shear bands can be expressed as:

$$ L = \frac{\Psi_i R_f}{n_i \sqrt{2}} \left(\frac{R_{f0}}{R_f} \right) \cong \frac{\sum_i L_{i,i-1}}{n_i} \left(\frac{R_{f0}}{R_f} \right), \qquad (21) $$

where R_{f0} is the radius of the specimen at shear band initiation, and R_f is the final radius, at any larger effective strain. $L_{i,i-1}$ is defined as the spacing between ith and $i-1$th shear bands in Fig. 4. Since $R_f < R_{f0}$, the corrected spacing based on the final configuration always has a lower value.

4. Microstructural characterization

There are significant differences between the two materials, in spite of their close composition and thermal properties. Fig. 5 shows the characteristic configuration of shear bands for Ti and Ti–6Al–4V. Three bands are seen in Fig. 5(a), whereas only one band is seen in Fig. 5(b); it should also be noted that the magnification in Fig. 5(a) is almost twice of that in Fig. 5(b). These results suggest (and this will be analytically developed in Section 6) that the interaction between nuclei of shear bands in Ti–6Al–4V is relatively weak. Each shear band grows fast once it nucleates. Unloading from a developed shear band during growth reduces new nucleation sites in the surrounding areas. The examination of the ratio of the lengths of shear bands and their edge displacement, $1/\delta$, also indicates the major difference between Ti and Ti–6Al–4V. $1/\delta$ is about 14.5 for Ti and 26.5 for Ti–6Al–4V at the same value of δ. This result clearly indicates that the shear bands develop much faster in
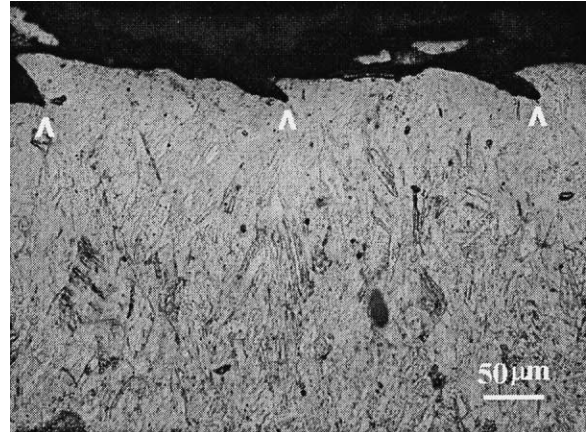

(a)
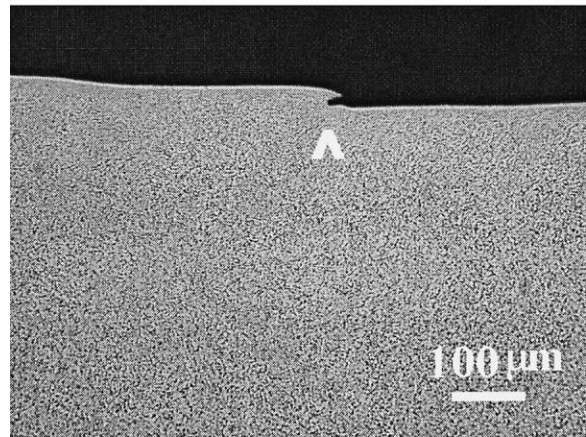
(b)

Fig. 5. Comparison of nucleation sites between Ti and Ti–6Al–4V alloy. (a) Titanium and (b) Ti–6Al–4V alloy.

Ti–6Al–4V alloy than in Ti. The detailed analysis of shear band development is presented in Section 6.

The thickness of the band was found to be a function of the distance from its tip. This holds for both materials and had been observed earlier by Nesterenko et al. [20] for Ti. The largest shear-band thickness in Ti is approximately 10 μm. The tip of the band reaches a level of intermittent localization in which the grain scale plays a role. This is seen in Fig. 6(a) in which the band (in Ti–6Al–4V) is shown by arrows. The thickness is on the order of 1 μm. There is a slight discontinuity,
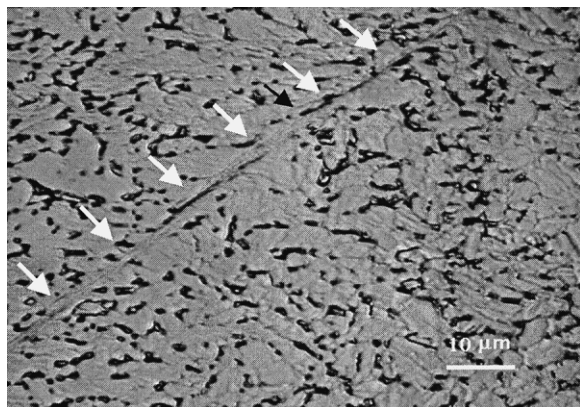
(a)
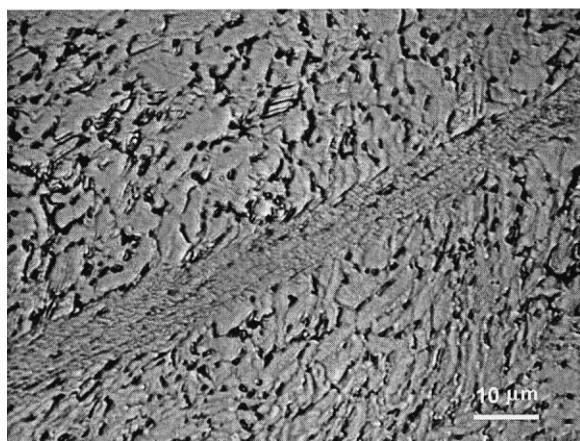
(b)

Fig. 6.   Evolution of shear band width and morphology in Ti–6Al–4V alloy: (a) fine tip section of the band; (b) well-developed section of the band.

marked by a black arrow. Fig. 5(b), on the other hand, shows a well-developed band. The thickness is approximately 8 µm. The interior is virtually featureless, and the original microstructure has been eliminated. It has been shown by Grebe et al. [37] for Ti–6Al–4V and by Meyers and Pak [11] and Meyers et al. [12] for Ti that the structure within the shear band consists, at a sufficiently high shear strain, of small (0.1–0.3 µm) equiaxed grains. The featureless material within the band was concluded to be the result of a rotational dynamic recrystallization instead of the product of phase transformation, as suggested by the early literature on shear

bands, based exclusively on optical microscopy observations. It is now recognized that a number of microstructural changes can and do occur within shear bands, including dynamic recovery and recrystallization, phase transformation and even amorphization. The presence of fine equiaxed subgrains within the shear band with the average diameter of 0.2 µm provided a direct evidence for dynamic recrystallization. However the deformation time is lower, by orders of magnitude, than the time required for boundary migration. Thus, a rotational mechanism, previously mentioned by Derby [38] in his classification of dynamic recrystallization, was proposed for the shear bands [39,40].

Another important feature of shear bands observed in the exploding cylinder geometry is the bifurcation. This bifurcation of bands is geometrically necessary due to the spiral trajectory of the bands, starting in the internal surface. In order to retain the same band spacing as they travel outwards, new bands have to be generated. Bifurcation is one possible means and it has been previously observed in steels (e.g. [41], Fig. 5). Fig. 7 shows a bifurcation event for Ti–6Al–4V.

Shear localization precedes failure mechanisms such as voids and cracks. A well-developed shear band is often accompanied with voids and cracks
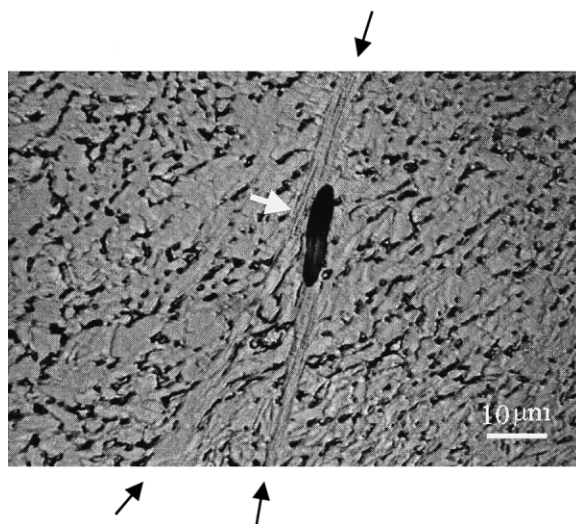

Fig. 7.   Shear band bifurcation and induced damage in Ti–6Al–4V alloy.

within it. These defects evolve and interact with shear bands during shear localization. Defects accelerate localization and localized deformation creates fresh nucleation of micro-voids and cracks.

The evolution of defects within shear bands in Ti–6Al–4V alloys showed, in this geometry, an entire range of events associated with damage and failure. The nucleation of micro-voids is considered as a result of the tensile stress inside shear bands. Void evolution is comprised of the three main stages: nucleation, growth, and coalescence. Fig. 8(a) shows nucleation stage of voids within shear bands. Three voids with circular or elliptical shape are initiated within shear band. All voids have smooth surfaces. It means that the material inside the band is quite soft and the temperature within the band is high. These voids nucleate completely inside the band and are surrounded by the

flow of localized deformation. They grow up with the localization progress in the growth stage. Most of voids first grow to the width of the band and then are elongated to elliptical shape along the direction of the shear band (see Fig. 8(b)). Further growth of these voids is accompanied with rotation along the shear direction. The second stage of void growth is characterized with the void elongation and rotation. Several voids are elongated to ellipse shape and rotated along direction of shear moment in Fig. 8(c). The third stage of void development is coalescence of voids and crack generation. Fig. 8(d) shows the whole process of void coalescence. These elliptical voids tilt their long axis to a certain angle coalescence of a group of voids inside shear band.

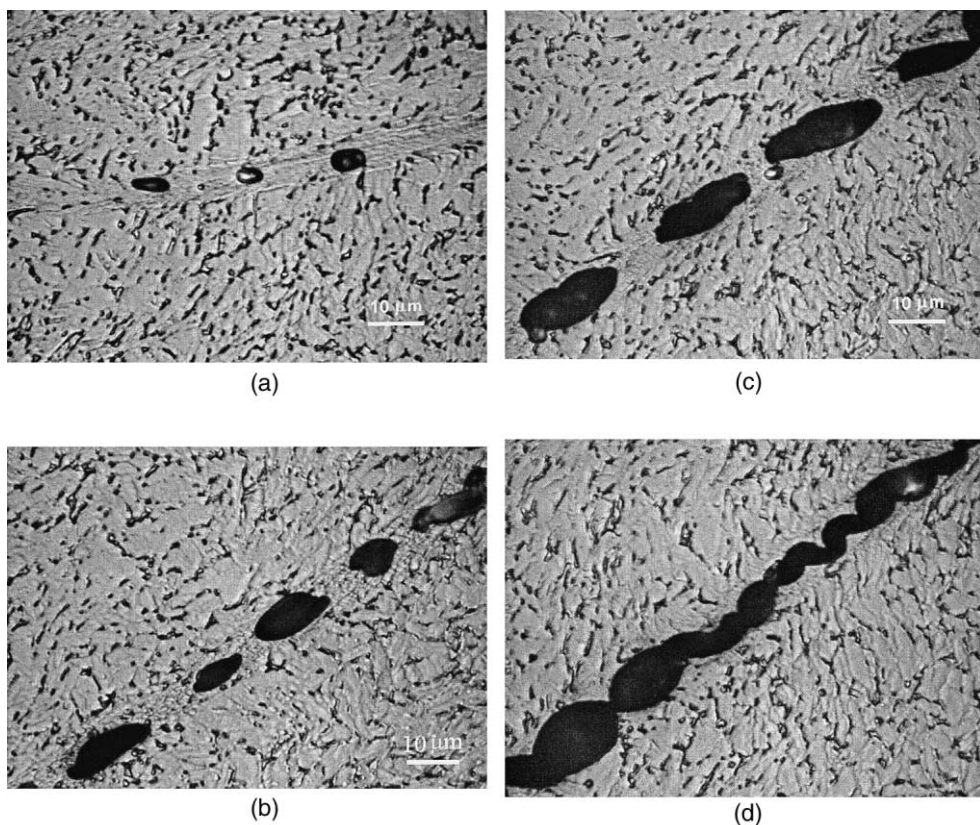Timothy and Hutchings [13,14] proposed a simple schematic plot to express the void evolution

Fig. 8.   Void nucleation and growth inside a shear band in Ti–6Al-4V alloy: (a) nucleation of voids within a shear band; (b) growth of voids; (c) elongation and rotation of voids; (d) coalescence.

within shear bands. A similar schematic descrip-
tion is presented in Fig. 9. Although there are some
differences in the details, the major processes in
their plot are in good agreement with what is
observed in Ti–6Al–4V alloy represented in Fig.
8. Voids nucleate within the shear bands when
there is tension. They grow until their edges reach
the boundary of the band, where the strength of the
material is higher due to the lower temperature.
Growth continues within the bands, and the voids
become elongated in the process. They can eventu-
ally coalesce, creating complete separation. This
process in the absence of shear strains is shown in
Fig. 9(a). If there are shear strains present concur-
rently with tension, the voids are elongated and
rotated. This is shown in Fig. 9(b). The ellipsoids
no longer share a common major axis. Their axes
are parallel and inclined to the shear-band plane.
In the present case a mixture of the two cases was
observed. The collapsed cylinder specimens move
continuously inward during the implosion process,
and only compressive and shear stresses are gener-
ated at this stage. During the unloading stages, ten-
sile circumferential stresses are generated in the
cylinders because of the radial dependence of the
stresses. These tensile stresses are responsible for
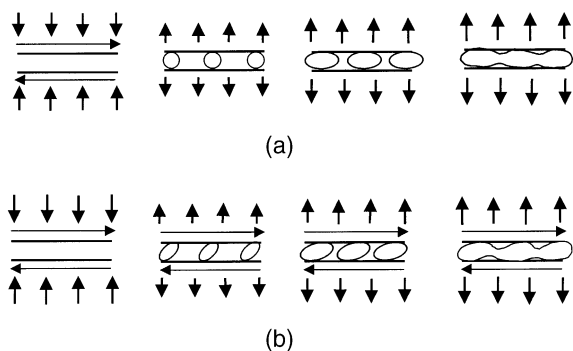further growth of voids generated within the bands.

(a)

(b)

Fig. 9. Schematic representation of void nucleation, growth,
and coalescence in (a) absence and (b) presence of continuing
shear.

5. Shear-band spacings
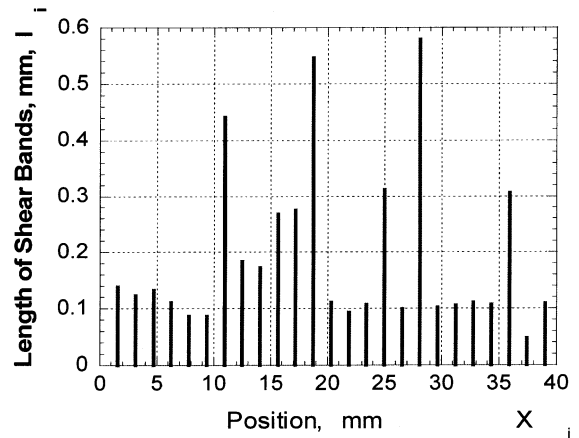
5.1. Titanium

In the present study, the titanium samples from
the experiments carried out by Nesterenko et al.
[20] were carefully re-examined by using both
optical microscopy and SEM. The configuration of
shear bands on the cross sections of the cylindrical
specimens was described before [20,34]. It consists
of spiral trajectories. The lengths, the edges and
spacing of shear bands were re-measured. Detailed
observation shows that there is a large number of
small shear bands that had not been counted in the
former work. The total number of shear bands in
CP titanium at this stage is 116, while the earlier
count [20] was 11. The large difference is due to
fact that emerging shear bands were neglected
earlier. At an effective strain of 0.92, the number
of shear bands is 108. The earlier count was 30.
The spectra of shear-band distribution at the two
strains are shown in Fig. 10. The numbers of shear
bands at both the early stage and the later stage
are similar. This implies that there is no new
nucleation of shear bands at the internal boundary
after an effective strain of 0.55. Only previously
nucleated shear bands grow between $\varepsilon_{ef} = 0.55$ and
$\varepsilon_{ef} = 0.92$. The spacing of shear bands in CP
titanium reaches a saturation state and remains
constant. The average shear band spacing is 0.18
mm. Fig. 10 shows that the number of bands grow-
ing at the strain of 0.92 is smaller than at 0.55; the
spacing is dependent on the size of the shear bands.
This size-dependent spacing necessitates a two-
dimensional treatment; this is done in Section 6.
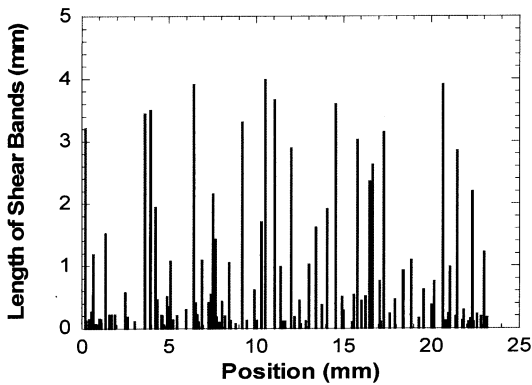
5.2. Ti–6Al–4V alloy

Four different effective strains were selected to
examine the evolution of the patterns of shear
localization. They are 0.13, 0.26, 0.55 and 0.92.
Shear localization is initiated at a much earlier
stage in Ti–6Al–4V alloy than in CP Ti. In com-
parison, at the same effective strains of 0.55 and
0.92 for Ti, the shear bands are much shorter [47].
A well-developed shear-band pattern is already
formed at an effective strain of 0.26. The numbers
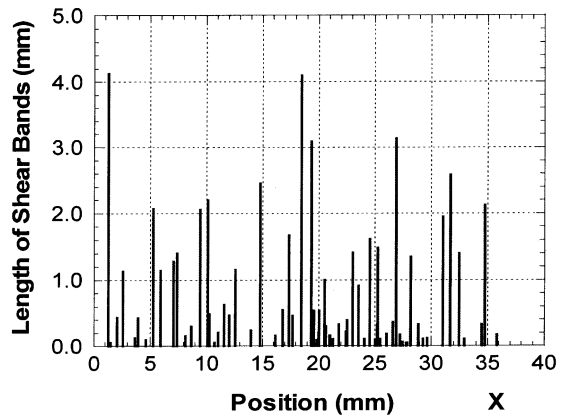of shear bands are: 68 for $\varepsilon_{ef} = 0.26$, 64 for
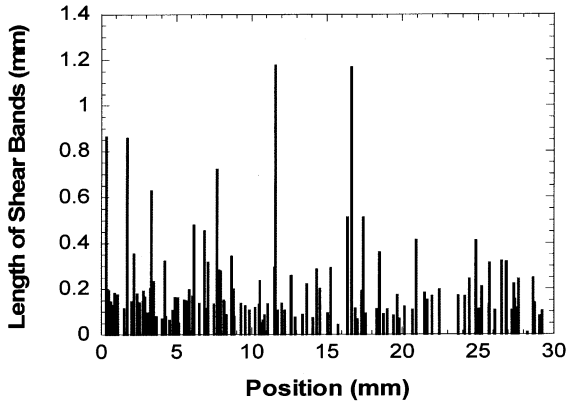
(a) Early Stage, ε_{ef} = 0.55, L = 0.18 mm, N = 114

(b) Late stage, ε_{ef} = 0.92, L = 0.18 mm, N = 108

Fig. 10. Spectra of shear band distribution in CP titanium at two different stages: (a) ε_{ef} = 0.55; and (b) ε_{ef} = 0.92.

(a)

(b)

Fig. 11. Spectra of shear bands distribution in Ti–6Al–4V alloy: (a) early stage (ε_{ef} = 0.13); (b) late stage, (ε_{ef} = 0.26).

ε_{ef} = 0.55, and 68 for ε_{ef} = 0.92. The numbers of shear bands remain approximately constant, indicating that once the shear band becomes well-developed, no further nucleation takes place. The shear band pattern at an early stage, at an effective strain of ε_{ef} = 0.13, gives a number of only 25. This strain is within the nucleation stage.

Fig. 11 shows the distribution of shear bands for two effective strains in Ti–6Al–4V alloy. The nucleation of shear bands occurs within a certain range of strains after a critical strain is reached. Two principal differences exist between the evol-

ution in Ti and Ti–6Al–4V. One is that the range of strains for nucleation in Ti–6Al–4V alloy appears to be broader than in titanium. The other is associated with the velocity of shear bands. The velocity can be estimated from the collapse velocity of the cylinder and the length of the bands. The total travel distance of the inner surface of the cylinder divided by the collapse velocity provides the propagation time. The calculation is carried out in Section 5.3. The spacing is, as for Ti, observed to increase with the size of the bands.

5.3. Propagation velocity of shear bands

The velocity of shear band propagation can be estimated from the experimental data of the collapsed cylinder tests. According to Nesterenko et al. [20,30,33], the average shear strain rate in the internal boundary of the thick-walled cylinder specimen is 3.5×10^4 s^{-1}. The corresponding radial strain rate, $\dot{\varepsilon}_{rr}$ is 1.75×10^4 s^{-1}. This corresponds to an average collapse velocity of 200 m/s. Radial strains at the two deformation stages can be transformed into the corresponding effective strains by using Eq. (19). For CP Ti, the radial strains are 0.476 and 0.797, corresponding to $\varepsilon_{eff} = 0.55$ and $\varepsilon_{eff} = 0.92$, respectively. For Ti–6Al–4V alloy, they are 0.113 and 0.225, corresponding to $\varepsilon_{eff} = 0.13$ and $\varepsilon_{eff} = 0.26$, respectively. The differences of duration between two strains are:

$$\Delta t = \frac{\Delta \varepsilon_{rr}}{\dot{\varepsilon}_{rr}} = \frac{\varepsilon_{rr2} - \varepsilon_{rr1}}{\dot{\varepsilon}_{rr}}, \qquad (22)$$

where the subscripts 1 and 2 represent the two stages of strain. The differences of duration are 18.3 μs for Ti and 6.46 μs for Ti–6Al–4V. The increments of the longest length of shear bands for these two materials are obtained directly from the data in Figs. 10 and 11. The maximum length of shear bands in Ti increases from 1.2 mm ($\varepsilon_{eff} = 0.55$) to 4.0 mm ($\varepsilon_{eff} = 0.92$), while that in Ti–6Al–4V increases from 0.58 mm ($\varepsilon_{eff} = 0.13$) to 4.18 mm ($\varepsilon_{eff} = 0.26$). The average velocities of shear band propagation are directly calculated and are equal to 153 m/s for Ti and 556 m/s for Ti–6Al–4V.

Zhou et al. [42,43] measured and numerically calculated the velocity of propagation of shear band in Ti–6Al–4V impacted at 64.5 m/s. The propagation velocities were 50–75 m/s, one order of magnitude less than the current results. It is concluded that the velocity of propagation of shear bands is dependent on the energy available for release at the front. The energy release rate for Ti–6Al–4V is significantly higher than for Ti due to its higher yield stress. This explains, qualitatively, its higher propagation velocity.

Mercier and Molinari [44] proposed a theoretical analysis for the velocity of propagation of shear bands incorporating some of these concepts. The band is evaluated in simple shear (Mode II). Fig. 12(a) shows the Mode II configuration used by Mercier and Molinari [44]. A slab with thickness $2h$ is sheared with top and bottom boundaries displaced at velocities C and $-C$, respectively. A shear band propagates in the center of the slab with velocity V. The band thickness is t and the process zone size is λ. Using a variational method, two variational relations were obtained as

$$\int_{-h}^{h} [\sigma_{xx}]_{-\infty}^{\infty} dy + \int_{-\infty}^{\infty} [s_{xy}]_{-h}^{h}$$

$$\qquad (23)$$

$$- \int_{-\infty}^{+\infty} \int_{-h}^{h} \left(s_{ij} \frac{\partial \dot{\varepsilon}_{ij}}{\partial V} + \rho a_i \frac{\partial v_i}{\partial V} \right) dx\, dy = 0,$$
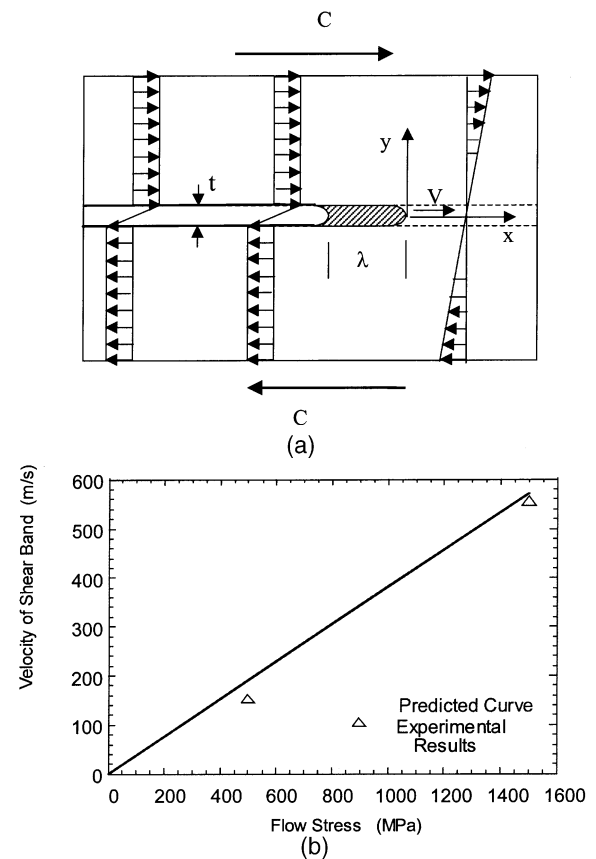

Fig. 12. Calculated propagation velocity for shear band, using Mercier and Molinari's [42] theory): (a) velocity configuration used in calculation; (b) predicted velocities for different conditions.

$$\int\limits_{-\infty}^{+\infty}\int\limits_{-h}^{h}\left(s_{ij}\frac{\partial\dot{\varepsilon}_{ij}}{\partial\lambda} + \rho a_i\frac{\partial v_i}{\partial\lambda}\right)dx\,dy = 0, \qquad (24)$$

where $a_i = v_{i,k}v_k$ ($i = 1,2$) is the acceleration of shear bands, and s_{xy} are the deviatoric Cauchy stresses. These relations were further simplified under the constrained condition. The velocity of shear band V and the characteristic length of the process zone λ can be obtained by the solution of following equations:

$$\int\limits_{-\infty}^{\infty}[s_{xy}(x,h) + s_{xy}(x,-h)-2s_{xy}(x,0)]dx \qquad (25)$$
$$-\rho CV(h-t) = 0,$$

$$-2\int\limits_{-\infty}^{+\infty}\int\limits_{-h}^{h}\left[x\left(s_{xx}\frac{\partial\dot{\varepsilon}_{xx}}{\partial x} + s_{xy}\frac{\partial\dot{\varepsilon}_{xy}}{\partial x}\right)\right.$$
$$\left. + s_{xx}\dot{\varepsilon}_{xx} + s_{xy}\frac{\partial v_y}{\partial x}\right]dx\,dy \qquad (26)$$
$$-\int\limits_{-\infty}^{+\infty}\int\limits_{-h}^{h}\rho xV\left[\left(\frac{\partial v_x}{\partial x}\right)^2 + \left(\frac{\partial v_x}{\partial y}\right)^2\right]dx\,dy$$
$$= 0.$$

For a rigid perfectly plastic material, an expression of the form was obtained by Mercier and Molinari [44]:

$$V = \frac{\sigma_f}{\rho C}g\left(\frac{\lambda}{h},\frac{t}{h}\right), \qquad (27)$$

where σ_f is the flow stress, ρ is the density. Thus, the shear band velocity is directly proportional to the flow stress. The value for the function $g(\lambda/h, t/h) = 0.343$ was obtained from Fig. 5 of Mercier and Molinari [44]. The predicted velocities are shown in Fig. 12(b). The velocity C was taken, to a first approximation, as 200 m/s. This is the initial collapse velocity for the cylinder. For the current results, the predicted velocities are 190.5 for Ti (σ_f = 500 MPa) and 571.5 m/s for Ti–6Al–4V (σ_f = 1500 MPa), respectively. The corresponding experimental velocities are 153 and 556 m/s, respectively. The calculated and experimentally

inferred results are in excellent agreement. The variational theory of Mercier and Molinari [44] predicts correctly the dependence of propagation velocity on flow stress.

5.4. Comparison of predicted and experimental results

The significant differences in shear-band spacing encountered in the two materials is surprising. It is indeed interesting to notice that these two materials, with fairly close compositions based on Ti, have such a dissimilar response. The physical and mechanical parameters for CP Ti and Ti–6Al–4V alloy are listed in Table 2. Using these parameters, the predicted spacings of shear bands from the three theoretical models presented in Section 2 can be calculated. The predictions for the three models are shown in Table 3. Since the Grady–Kipp model does not consider the strain rate effect, the shear yield stresses in this model correspond to those under dynamic loading condition. The WO and Molinari (without work hardening) models give predictions for Ti as L_i = 0.29 mm and L_i = 0.24 mm, respectively. The experimental results show that the spacing of shear bands is 0.18 mm. The predictions are reasonably close to the observed spacing. The GK model predicts the shear band spacing to be 2.13 mm, which is much larger. Thus, the predictions of WO/Molinari models are in approximate agreement with the observed shear band spacing in CP titanium. If work hardening is incorporated into the Molinari model, the predicted spacing increases somewhat. The Molinari equation is applied in its simplified, non-work hardening form (Eq. (15)) and in the form given below, which uses a softening term different from the original formulation for ease of mathematical manipulation. The following constitutive equation was used:

$$\tau = \mu_0(\gamma + \gamma_i)^n\,\dot{\gamma}^m(1-aT). \qquad (28)$$

The corresponding spacing is

$$L_M = L_0\left[1-\frac{3}{4}\frac{\rho c}{\beta\tau_0}\frac{n(1-aT)}{a\gamma}\right]^{-1}, \qquad (29)$$

L_0 is the spacing for the non-work hardening case.

Table 2
Physical and mechanical parameters for prediction of shear-band spacing[a]

Material	Density	Heat capacity	Thermal conductivity	Thermal softening factor	Strain rate hardening index
	ρ (g/cm³)	C (J/kg K)	k (W/mK)	a (K^{-1})	M
Titanium	4.51	528	16.44	10^{-3}	0.027
Ti–6Al–4V	4.43	564	3.07	10^{-3}	0.017
	Strain hardening index	Shear stress	Dynamic shear stress	Shear strain rate	
	n	(MPa)	(MPa)	$\dot{\gamma}$ (s^{-1})	
Titanium	0.18	180	280	6×10^4	
Ti–6Al–4V	0.15	490	650	6×10^4	

[a] Thermal properties and densities are from Ref. 50; thermal softening factor from Nesterenko et al. [20]; other parameters from experimental data.

Table 3
Comparison of shear band spacings between the experimental results and theoretical predictions

Spacing (mm)	Experimental data	Grady–Kipp	Wright–Ockendon	Molinari (without strain hardening)	Molinari (with strain hardening effect)
CP titanium	0.18	2.13	0.29	0.24	0.64
Ti–6Al–4V alloy	0.53	1.15	0.10	0.09	0.10

The predicted spacing is increased from 0.24 mm to 0.64 mm.

The number of shear bands for Ti–6Al–4V alloy is essentially constant for the global effective strains 0.26, 0.55 and 0.92; an average number can be taken as approximately 66. The corresponding spacing of shear bands is $L_i = 0.526$ mm. Therefore, it can be concluded that after this spacing is reached, no further nucleation occurs. The predicted results for shear band spacing are also shown in Table 3. The values of spacing for WO and Molinari models are 0.10 mm and 0.09 mm, respectively. Thus, the experimental results are roughly 5 times the theoretical predictions. On the other hand, the GK model predicts a spacing $L = 1.15$ mm, which is roughly double the experimental results. So, the experimental and calculated spacings do not show as good an agreement as in Ti. Moreover, the proposed models do not predict observed tendency in shear band spacing between titanium and Ti–6Al–4V.

The failure of these theoretical predictions in Ti–6Al–4V alloy suggests that some mechanisms of shear band development have not been included into the current models. Considering the Molinari model with work hardening, the strain hardening is 0.15 for the Ti–6Al–4V alloy, which is lower than the one for Ti. The incorporation of this strain hardening index cannot result in a substantial change of the spacing of shear bands. Therefore, strain hardening should not be the main reason for the failure of the prediction.

The Grady–Kipp model overestimates the spacing considerably, whereas WO and M models underestimate it. Section 6 will present a two-dimensional model in which shielding is incorporated into the nucleation.

The temperature increment due to deformation can be estimated through the predictive constitutive relations. This temperature rise helps to explain some of the differences in shear bands between the two materials. The temperature change is given by:

$$\frac{dT}{dt} = \beta\frac{\sigma\dot{\varepsilon}}{\rho C(T)}, \tag{30}$$

$$\int_{T_0}^{T}\frac{\rho C(T)}{\beta\sigma(T)}dT = \int_{0}^{t}\dot{\varepsilon}dt = \int_{0}^{\varepsilon}d\varepsilon = \varepsilon. \tag{31}$$

The stress as the function of temperature, $\sigma(T)$, is obtained directly from the Zerilli–Armstrong equation (Eq. (16)). The heat capacities $C(T)$ are:

$$\text{CP Ti} \quad C(T) = 0.514 + 1.357\times10^{-4}\,T$$
$$-\frac{3.366\times10^3}{T^2}$$
$$+ 2.767\times10^{-8}\,T^2[\text{J/kgK}] \tag{32}$$

$$\text{Ti-6Al-4V} \quad C(T) = 0.559$$
$$+ 1.357\times10^{-4}\,T - \frac{3.366\times10^3}{T^2}$$
$$+ 2.767\times10^{-8}\,T^2[\text{J/kgK}] \tag{33}$$

In the adiabatic case ($\beta = 1$), numerical integration of Eq. (31) gives the relation between strain and temperature increment. Fig. 13(a) shows the temperature as a function of effective strain for the two materials. The temperature rises faster for Ti–6Al–4V. The effective strains corresponding to the initiation of localization, approximately 0.5 and 0.3, correspond to the same temperature rise of 100 K. A greater plastic deformation is needed to increase the temperature to the same level in Ti. Culver [45] introduced a simple relation between true strain and engineering shear strain.

$$\varepsilon = \ln\sqrt{1 + \gamma + \frac{\gamma^2}{2}} \tag{34}$$

$$\gamma = \sqrt{2e^{2\varepsilon}-1}-1 \tag{35}$$

It should be mentioned that his conversion relation is for simple shear case, although, strictly speaking, the state of stress in these experiments is of pure shear. The relations between temperature and the converted engineering shear strain are plotted in Fig. 13(b). The temperature corresponding to $T_m/2$ (one half the melting temperature) is an approximate measure of the onset of recrystallization. It is marked in Fig. 13(b). It represents shear strains of 5 and 3 for Ti and Ti–6Al–4V, respectively. The shear strains in the bands can be esti-
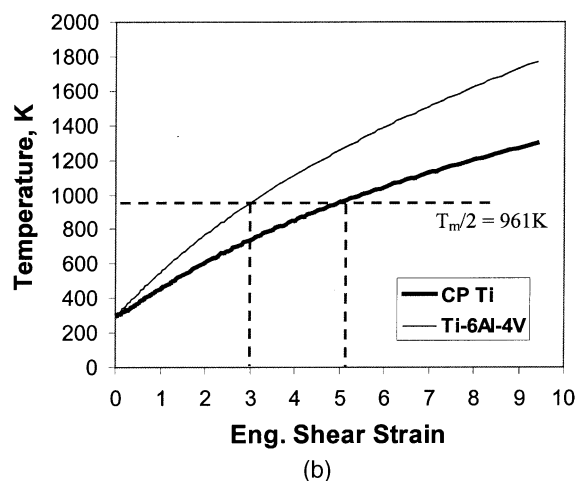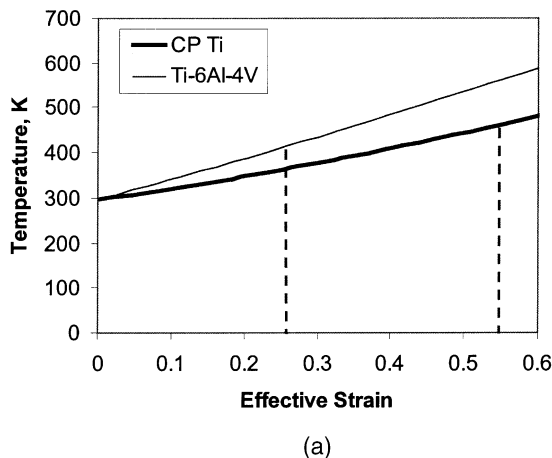

(a)

(b)

Fig. 13. Predicted temperature for CP titanium and Ti–6Al–4V alloy (a) as a function of effective strain γ, and (b) as a function of shear strain.

mated from the edge length/thickness (δ/t) ratios. The typical edge length in the Ti–6Al–4V specimen at a global strain of 0.13 is about 30 μm at $\varepsilon_{ef} = 0.26$ and the typical thickness of the shear band is 8 μm. This gives a shear strain about 4. At a more advanced stage (global strains of 0.26 and 0.55) the edge lengths are about 0.33 mm and 1.67 mm, respectively. These correspond to strains of 41 and over 200, respectively. These are vastly superior to the recrystallization temperature and could even generate melting.

6. Two-dimensional effects among multiple shear bands

The failure of the one-dimensional models to explain the evolution of shear-band spacing led to the considerations outlined below. In order to describe such self-organization behavior two basic processes, initiation and growth, need to be included separately. Initiation can be treated as the selective activation of sites. Growth represents the competition among bands and interaction during the propagation stage.

The three important factors that determine the development of spacing of shear bands are: (a) the rate of initiation, (b) the rate of growth (or the velocity of shear bands), and (c) characteristic time of interaction between shear bands.

6.1. Initiation stage

Shear bands nucleate at the internal boundary of the specimen. The initiation sites are determined by the small perturbations of initial deformation. They may be located at favorably oriented grains and defects. Initiation of shear bands requires a critical strain at a certain stress. Heterogeneous microstructural or surface effects (boundary geometry, defects, orientation of grains, etc.) determine the range of strains in which the nucleation takes places. We will treat the initiation like a nucleation process. In heterogeneous nucleation theory, the term embryo is used as a potential nucleation site. The rate of nucleation of bands is associated with a plastic strain rate, $\dot{\varepsilon}$.

The probability of nucleation is given by $P(V_0, S_0)$, in a reference volume, V_0, or surface, S_0, depending whether initiation occurs in the bulk or on the surface. It can be described by a modified Weibull [46] distribution, using strain as the independent variable (in lieu of stress, in the conventional approach). Thus,

$$P(V_0, S_0) = 1 - \exp\left[-\left(\frac{\varepsilon - \varepsilon_i}{\varepsilon_0 - \varepsilon_i}\right)^q\right], \qquad (36)$$

where ε_i is the critical strain below which no initiation takes place; ε_0 is the average nucleation strain (material constant); ε is the variable; and q is

a Weibull modulus. The different Weibull moduli reflect the dispersion of shear band nucleation. For different materials the nucleation curve can have different shapes and positions, adjusted by setting q, ε_i, and ε_0. The rate of nucleation can be obtained by taking the time derivative of the above expression. In the geometry used in the experiments, the initiation occurs on the inside surface of the cylinder. For Ti and Ti–6Al–4V, the average nucleation strains are selected as 0.4 and 0.12, respectively, to best fit the experimental results; q was given values of 2, 3, 6, and 9, providing different distributions. Figs. 14(a) and (b) show the predicted distributions of initiation strains for Ti and Ti–6Al–4V, respectively.

There is also a continuing shielding effect, so that the bands that actually grow can be a fraction of the total possible initiation sites. Fig. 15 shows the schematic interaction between embryos and growing shear bands. Each growing band generates a shielded region around itself, that is the result of unloading.

The factors governing the evolution of self-organization include: (a) the strain rate, $\dot{\varepsilon}$; (b) the velocity of growth of shear band, V; (c) the initial spacing, L.

Different scenarios emerge, depending on the growth velocity V. The shielded volume is dependent on the velocity of propagation of stress unloading and is directly related to the momentum transfer used by Grady and Kipp [21]; this is given by $k_1 V$, where $k_1 < 1$. If the unloading velocity were equal to the propagation velocity, one would have
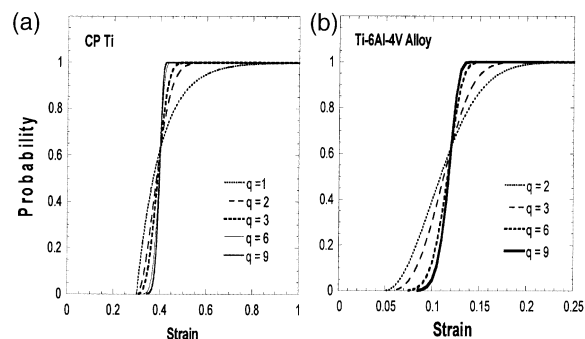

Fig. 14. Probability of nucleation of shear bands in Ti (a) and Ti–6Al–4V (b) as a function of shear strain for four values of q: 2, 3, 6, and 9.
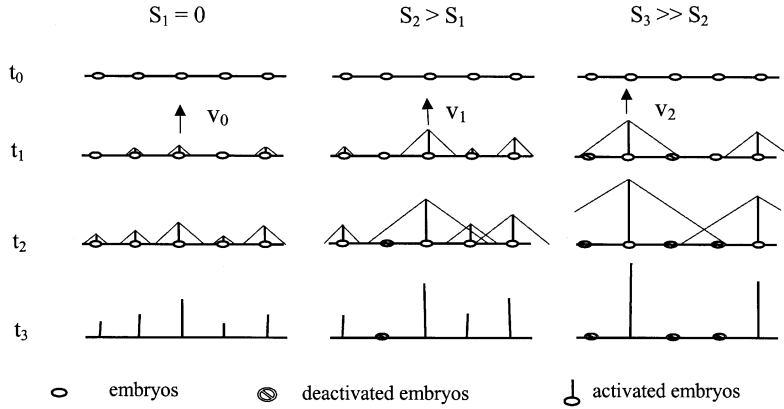
Fig. 15. Two-dimensional representation of concurrent nucleation and shielding.

$k_1 = 1$. The activation of embryos at three times, t_1, t_2, and t_3, is shown in Fig. 15. When V is low, the embryos are all activated before shielding can occur, and the natural spacing L establishes itself. As V increases, shielding becomes more and more important, and the number of deactivated embryos increases. For a full nucleation case, the predicted spacing of shear bands in Ti is roughly 0.24 times of the maximum length of shear bands. The width of the unloaded region is $2k_1$ times the length of the shear band.

The shielding effect can be expressed by S:

$$S = 1 - \frac{\dot{\varepsilon}L}{k_0 k_1 V}. \tag{37}$$

The parameter k_0 defines the range of strains over which nucleation occurs. It can be set as $2(\varepsilon_0 - \varepsilon_i)$:

$$k_0 = 2(\varepsilon_0 - \varepsilon_i). \tag{38}$$

The physical meaning of the shielding factor S is determined by the ratio of two characteristic times. One is the characteristic time for complete nucleation, $\bar{t}$:

$$\bar{t} = \frac{k_0}{\dot{\varepsilon}} = \frac{2(\varepsilon_0 - \varepsilon_i)}{\dot{\varepsilon}}. \tag{39}$$

The other characteristic time is $t_s = \bar{t} - t_{cr}$, where t_{cr} is a critical time at which complete shielding occurs:

$$t_{cr} = \frac{L}{k_1 V}. \tag{40}$$

It is assumed that the nuclei that have not been activated after t_{cr} can no longer be initiated. Therefore, the shielding factor is defined as:

$$S = \frac{\bar{t} - t_{cr}}{\bar{t}}. \tag{41}$$

This expression correctly predicts an increase in shielding S with increasing V, decreasing $\dot{\varepsilon}$, and decreasing L. For an extremely large velocity of propagation of shear band, the critical time is very small and the shielding factor is close to one, which means almost complete shielding. The probability of nucleation under shear band shielding, $P(L)$, is obtained by combining Eq. (37) and Eq. (36):

$$P(L) = \tag{42}$$
$$\begin{cases} (1-S) \cdot P(V_0, S_0) = \left(\dfrac{\dot{\varepsilon}L}{2(\varepsilon_0 - \varepsilon_i)V}\right)\left\{1 - \exp\left[-\left(\dfrac{\varepsilon - \varepsilon_i}{\varepsilon_0 - \varepsilon_i}\right)^q\right]\right\} & \text{if } t_{cr} < \bar{t} \\[2ex] P(V_0, S_0) = \left\{1 - \exp\left[-\left(\dfrac{\varepsilon - \varepsilon_i}{\varepsilon_0 - \varepsilon_i}\right)^q\right]\right\} & \text{if } t_{cr} \geq \bar{t} \end{cases}$$

When $S = 0$ no shielding effect exists and all nuclei grow. If, in the other extreme case, $S = 1$, no nucleation can happen. Fig. 16(a) shows predicted evolutions of nucleation probabilities as a function of increasing strain, for different values of the shielding factor, S: 0, 0.2, 0.4, 0.6. This simple model has the correct physics and shows how the initial distribution of activated embryos can be affected by different parameters. Xue et al. [47] and Nesterenko et al. [48] present a preliminary, simplified version of this analysis. It explains,
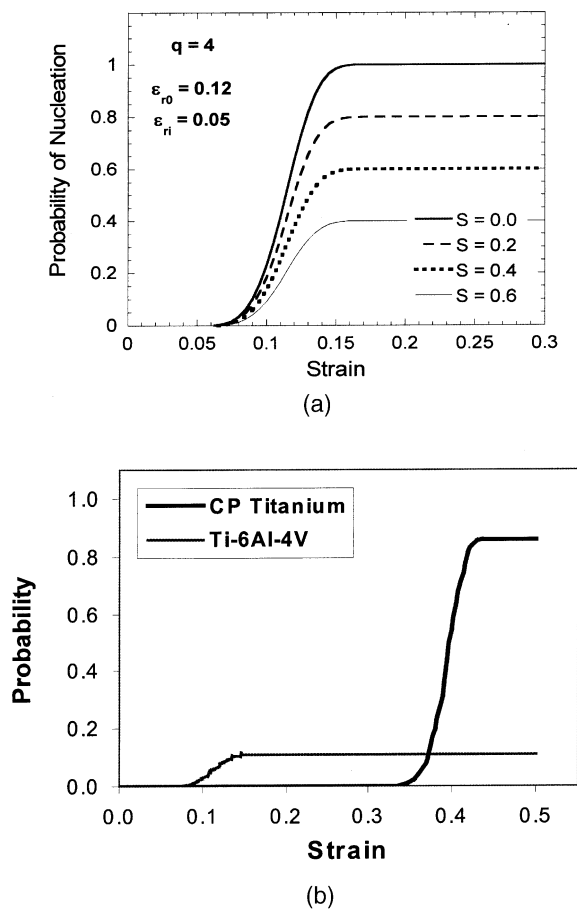
(a)

(b)

Fig. 16. (a) Effect of shielding on the probability of nucleation as a function of plastic strain (different values of shielding, S, given in plot). Representative values for Ti–6Al–4V. (b) Probability of nucleation of shear bands (incorporating calculated shielding factor S) for Ti ($q=6$, $S=0.14$) and Ti–6Al–4V ($q=4$, $S=0.89$).

qualitatively, the smaller spacing of shear bands in Ti, as compared to Ti–6Al–4V. Fig. 16(b) shows the predictions for these two materials. Applying Eq. (37), we obtain the shielding factors for the two cases. The following values were used: $V=153$ and 556 m/s for Ti and Ti–6Al–4V, respectively; $\dot{\varepsilon}_{rr} = 1.75{\times}10^4\ s^{-1}$; $\varepsilon_i - \varepsilon_0 = 0.1$ and 0.07 for Ti and Ti–6Al–4V, respectively; the range is numerically larger in Ti than in Ti–6Al–4V. In comparison with experimental observations, spacings $L = 0.29$ mm for Ti and $L = 0.1$ for Ti–6Al–4V are obtained from the Wright–Ockendon perturbation analysis

(Table 3). The ratio of the unloading velocity and the velocity of shear band, k_1, is taken as 0.2. It is recognized that these values are only approximate. The resultant shielding factors S are 0.14 for Ti and 0.89 for Ti–6Al–4V. Nevertheless, they provide a good estimate of the evolution of nucleation for the two cases. Fig. 16(b) shows that the spacing of shear bands is far from reaching saturation in Ti–6Al–4V due to significant shielding, whereas this effect is not so pronounced for Ti.

The shear-band spacing, corrected for shielding, is represented by:

$$L_s = \frac{L_{WO}}{P(L)|_{t>\bar{t}}} = \frac{L_{WO}}{(1-S)}. \qquad (43)$$

L_{WO} is the Wright–Ockendon spacing. This spacing is plotted as a function of S in Fig. 17(a) and as a function of plastic strain, at a fixed value of S, in Fig. 17(b). It is clear that the shear-band spacing decreases with strain until a final, steady state value is reached (Fig. 17(b)). Using the calculated shielding factors S of 0.14 for Ti and 0.89 for Ti–6Al–4V, the corresponding values for L_s are 0.34 and 0.9 mm, respectively. These values only approximate the experimental results (0.18 and 0.53 mm, respectively) but they have the correct trend, i.e. the spacing for Ti–6Al–4V is larger than for Ti. This eliminates the incorrect predictions of WO and M models where the spacing between shear bands in Ti–6Al–4V is smaller than in Ti. Considering the uncertainties of experiments and measurements, it is felt that the agreement is satisfactory.

6.2. Growth stage

It was observed in experiments that growing shear bands form an approximately periodical pattern. This is called a self-organization phenomenon.

Further deformation produces heterogeneous growth of these shear bands: some shear bands grow faster than others. The favorably loaded shear bands grow faster, while the unloaded shear bands slow down, and finally stop. The 'living' shear bands compete each other and construct a new spatial pattern by following the self-organization rule. The dead small shear bands may be left at their
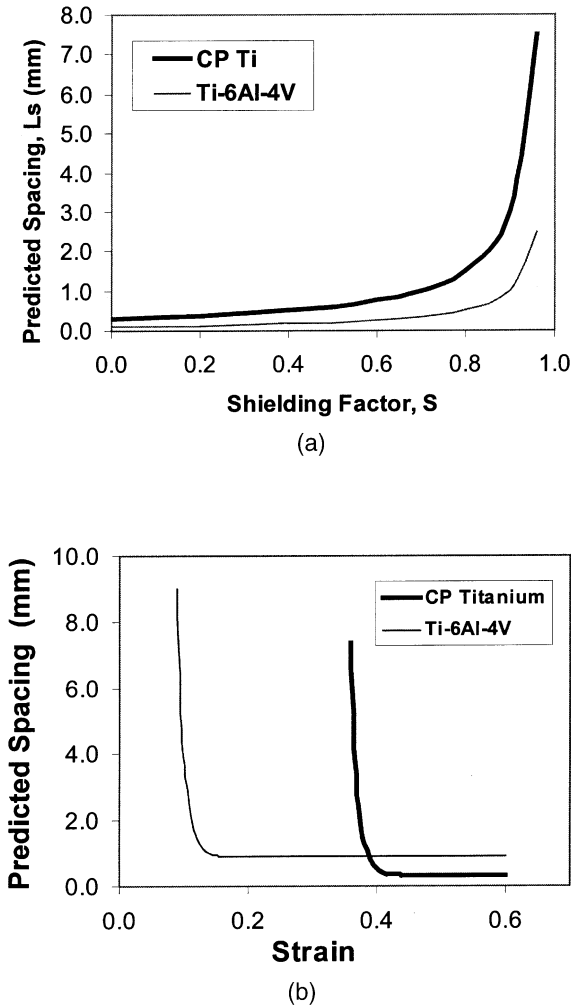
(a)

(b)

Fig. 17. Predicted shear-band spacing, L_s, as a function of (a) shielding factor S at large strain; and (b) strain with constant S.

original locations, or may be merged into the large plastic deformation of the surrounding area. In the latter case the apparent number of shear bands is effectively reduced.

The dominant factors in this process depend on the material parameters, constitutive character, loading condition, and strain rate. The velocity of shear bands, relative to unloading, is an important factor that affects their spatial distribution, an aspect which the current theories have not covered. In the extreme case when time of propagation of shear band through the specimen is smaller than

the characteristic time of shear band interactions, no self-organization during growth will take place.

The driving force for shear-band propagation is the release of elastic energy. The rate of nucleation is quite different from the growth rate (or growth velocity). It is reasonable to assume that the growth is governed by stress, whereas initiation is governed by strain. The necessary condition is:

$$\tau_g < \tau_i, \tag{44}$$

where τ_g and τ_i are the critical shear stresses for growth and initiation, respectively. The greater the difference, the higher the velocity of propagation. The unloading waves sweep through the surrounding area of a shear band and make any new nucleation impossible within this area.

The interaction of shear bands leads to the competitive growth of the propagating shear bands. The volume of material shielded from further nucleation and growth increases with the length of a shear band in cylindrical geometry and is not constant, as predicted with these elements in place, one can construct a more realistic two-dimensional theory for the evolution of the self-organization of shear bands.

Different evolution stages for shear bands are schematically indicated in Fig. 18. At a certain length l_i, the spacing is L_i. The growth becomes unstable at a critical length $l_{cr,i}$, and alternate shear bands grow with a new spacing L_{i+1}; the other shear bands stop growing. The mathematical representation of the step function shown in Fig. 13 is

$$L = L_0 + \sum_{j=1}^{n} k'_j \cdot H(l - l_{cr,j}), \tag{45}$$

where $H(l - l_{cr,i})$ is a Heaviside function. The parameters k'_j can be expressed as:

$$k'_j = f(V, L_0, \varepsilon_i, \varepsilon_p), \tag{46}$$

where V is the shear band propagation velocity, L_0 is the initial spacing, ε_i is the critical strain for initiation and ε_p is the critical strain for propagation. A similar phenomenon was observed and analyzed by Nemat Nasser et al. [49] in the fracture of glass. Thermal stresses were used to drive parallel cracks. As their length increased, their spacing would also increase. This occurred in a discontinuous manner.
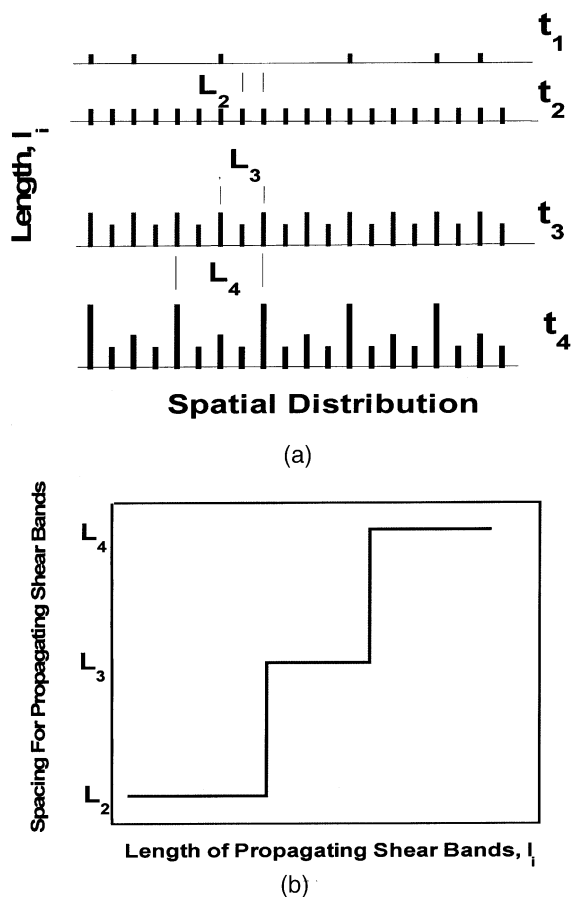
Fig. 18.   (a) Schematic diagram of the evolution of shear-band spacing at different levels: t_1, random initiation; t_2, self-organization into 'periodic' pattern among nuclei; t_3, some shear bands grow faster, suppressing others; t_4, self-organization of developed shear bands. (b) Spacing of propagating shear bands as a function of length.

7. Conclusions

Collective organization processes take place during the formation of shear bands. All the current theories on prediction of spacing of shear bands are based on one-dimensional analyses of shear bands. Therefore, it is no surprise that the current theories cannot explain the self-organization behavior of shear bands when they grow into two and three dimensional patterns.

The evolution of multiple adiabatic shear bands was investigated in commercially pure titanium and Ti–6Al–4V alloy through a radial collapse technique of a thick-walled cylinder under high-strain-rate deformation. Shear-band initiation, propagation, as well as spatial distribution were examined under different global strains. The shear bands nucleate at the internal boundary of the specimens and construct a periodical distribution at an early stage. The shear bands undergo bifurcation as they progress in their spiral trajectory and as their spacing increases. The shear bands are favored initiation sites for failure, which occurs by void nucleation, growth, and coalescence inside the thermally softened regions. The evolution of the morphology of the voids is determined by the restrictions imposed by the bands.

The evolution of shear-band pattern during the deformation process reveals a self-organization character. The differences of mechanical response between the two alloys are responsible for significant differences in the evolution of the shear band patterns. The number of shear bands initiated in Ti (spacing of 0.18 mm) is considerably larger than in Ti–6Al–4V (spacing of 0.53 mm); on the other hand, the propagation velocity of the bands in Ti–6Al–4V ($V{\sim}556$ m/s) is approximately three times higher than in Ti ($V{\sim}153$ m/s). The propagation velocities are successfully compared with values predicted from a variational analysis developed by Mercier and Molinari [44]. The experimentally obtained shear-band spacings are compared with theoretical predictions by Grady and Kipp [21], Wright and Ockendon [22], and Molinari [23] and the shortcomings of the predictions are discussed. The experimental results presented here for Ti and Ti–6Al–4V corroborate the earlier results [20] that self-organization is an important phenomenon in deformation by shear-band propagation. However, the shear-band interactions are more complex than previously thought and their spacing cannot be predicted by the one-dimensional perturbation theories of Wright and Ockendon [22] and Molinari [23]. The Grady–Kipp theory cannot accommodate the increased spacing as the shear-band size increases, since it is also one-dimensional. The proposed two dimensional model correctly describes the differences of spacings between behaviors of Ti and Ti–6Al–4V. It incorporates elements that are outlined below:

1. Rate of nucleation of shear bands. The probability of nucleation, $P(V_0,S_0)$, in a reference volume V_0, or surface S_0 was successfully described by a Weibull [46] distribution in which the stress was replaced by strain as the independent variable. Parameters defining the distribution are a critical strain for nucleation, a mean nucleation strain, and a Weibull modulus. There can also be shielding at the nucleation stage, depending on the relative values of the rate of nucleation and rate of growth.

2. Rate of growth, or velocity of propagation. This is an important factor in their self organization. Shear bands compete among themselves and gradually change their patterns. A 'Darwinian' natural selection takes place, and a large number of small bands evolves gradually into a smaller number of large bands, due to the shielding of stresses produced during growth. Such evolution of shear band pattern occurs under a homogeneously distributed pressure acting on the external boundary of the cylindrical specimen. This is a typical self-organization process among "aging" population of shear bands.

Acknowledgements

References

[1] Bai Y, Dodd B. Adiabatic shear localization. Oxford: Pergamon, 1992 p. 24.
[2] Meyers MA. Dynamic behavior of materials. J. Wiley, 1994 Chapter 15.
[3] Clifton RJ. In: Material response to ultra high loading rates. NRC Report No. 356, Washington (DC): US National Material Advisory Board; 1980. Chapter 8.
[4] Bai Y. In: Meyers MA, Murr LE, editors. Shock waves and high-strain-rate phenomena in metals, New York: Plenum Press; 1981:277.
[5] Molinari A, Clifton RJ. J Appl Mech 1987;54:806.
[6] Wright TW. Int J Plasticity 1992;8:583.
[7] Wright TW, Walter JW. J Mech Phys Solids 1987;32:119.
[8] Marchand A, Duffy J. J Mech Phys Solids 1988;36:261.
[9] Me-Bar Y, Shechtman D. Mater Sci Eng 1983;58:181.
[10] Grebe HE, Pak H-r, Meyers MA. Metall Trans 1985;16A:761.
[11] Meyers MA, Pak H-r. Acta Metall Mater 1986;34:2493.
[12] Meyers MA, Subhash G, Kad BK, Prasad L. Mech Mater 1994;17:175.
[13] Timothy SP, Hutchings IM. Acta Metall 1985;33:667.
[14] Timothy SP. Acta Metall 1987;35:301.
[15] da Silva MG, Ramesh KT. Mater Sci Eng A 1997;232:11.
[16] Chichili DR, Ramesh KT, Hemker KJ. Acta Mater 1998;46:1025.
[17] Chichili DR, Ramesh KT, Hemker KJ. In: Ankem S, Pande CS, editors. Advances in Twinning. Proceedings of an International Symposium. 1999 TMS Annual Meeting, TMS—Minerals, Metals & Materials Society; 1999:187.
[18] Bowden PB. Phil Mag 1970;22:455.
[19] Shockey DA. In: Murr LE, Staudhammer KP, Meyers MA, editors. Metallurgical applications of shock wave and high-strain-rate phenomena, New York: Marcel Dekker; 1986:633.
[20] Nesterenko VF, Meyers MA, Wright TW. Acta Mater 1998;46:327.
[21] Grady DE, Kipp ME. J Mech Phys Solids 1987;35:95.
[22] Wright TW, Ockendon H. Int J Plasticity 1996;12:927.
[23] Molinari A. J Mech Phys Soc 1997;45:1551.
[24] Grady D. J Geophys Res 1980;85:913.
[25] Mott NF. Proc R Soc 1947;189:300.
[26] Zerilli FJ, Armstrong RW. In: AIP Conference Proceedings (no. 370), Shock Compression of Condensed Matter, Seattle (WA), 1995, AIP; 1996. p. 31-5.
[27] Zerilli FJ, Armstrong RW. J Appl Phys 1987;61:1816.
[28] Zerilli FJ, Armstrong RW. J Appl Phys 1990;68:1580.
[29] Nesterenko VF, Lazaridi AN, Pershin SA. Fiz. Goreniya Vzryva 1989; 25:154 (in Russian).
[30] Nesterenko VF, Bondar MP. DYMAT J 1994;1:245.
[31] Shih CJ, Nesterenko VF, Meyers MA. J Appl Phys 1998;83:4660.
[32] Chen HC, LaSalvia JC, Nesterenko VF, Meyers MA. Acta Mater 1998;46:3033.
[33] Nesterenko VF, Bondar MP, Ershov IV. In: Schmidt SC, editor. High-Pressure Science and Technology—1993, AIP Conference Proceedings 309, New York: AIP Press; 1994:1173.
[34] Meyers MA, Wang SL. Acta Metall 1988;36:925.
[35] Kennedy JE. In: Behavior and Utilization of Explosives in Engineering Design, 12th Annual Symposium, Albuquerque (NM): ASME; 1972.
[36] Nesterenko VF, Meyers MA, Wright TW. In: Murr LE et al., Editors. Metallurgical and Materials Applications of Shock-Wave and High-Strain-Rate Phenomena, Oxford, UK: Elsevier, 1995: 397.
[37] Grebe HA, Pak Hr, Meyers MA. Metall Trans 1985;16A:711.

[38] Derby B. Acta Mater 1991;39:955.

[39] Meyers MA, LaSalvia JC, Nesterenko VF, Chen YJ, Kad BK. In: McNelley TR, editor. Recrystallization and Related Phenomena. ReX'96, Monterey, CA, 1997:279.

[40] Meyers MA, Nesterenko VF, LaSalvia JC, Xue Q. Mater Sci Eng 2001;A317:204.

[41] Wittman CL, Meyers MA, Pak H-r. Metall Trans 1990;21A:707.

[42] Zhou M, Rosakis AJ, Ravichandran G. J Mech Phys Solids 1996;44:981.

[43] Zhou M, Ravichandran G, Rosakis AJ. J Mech Phys Solid 1996;44:1007.

[44] Mercier S, Molinari A. J Mech Phys Soc 1998;46:1463.

[45] Culver RS. In: Rohde RW, Butcher BM, Holland JR, Karnes CH, editors. Metallurgical effects at high strain rates, New York: Plenum Press; 1973:519.

[46] Weibull W. J Appl Mech 1951;18:293.

[47] Xue Q, Nesterenko VF, Meyers MA. In: Staudhammer KP, Murr LE, Meyers MA, editors. Shock-wave and high-strain-rate phenomena, Oxford, UK: Elsevier; 2000:549.

[48] Nesterenko VF, Xue Q, Meyers MA. J Phys IV (Proc. EURODYMAT 2000) 2000;10:9–269.

[49] Nemat-Nasser S, Keer LM, Parihar KS. Int J Solids Struct 1978;14:409.

[50] Donachie Jr. MJ. Titanium and titanium alloys. Metal Park: ASM Press, 1982 p. 3.